

1 **Title: Structural basis of PROTAC cooperative recognition for selective protein**
2 **degradation**

3 **Authors:** Morgan S. Gadd¹, Andrea Testa¹, Xavier Lucas¹, Kwok-Ho Chan, Wenzhang
4 Chen, Douglas J. Lamont, Michael Zengerle, Alessio Ciulli*

5 **Affiliation:** Division of Biological Chemistry and Drug Discovery, School of Life Sciences,
6 University of Dundee, Dow Street, Dundee, DD1 5EH, Scotland, UK.

7 *To whom correspondence should be addressed. E-mail: a.ciulli@dundee.ac.uk

8 ¹ These authors contributed equally to this work

9 **Abstract:**

10 Inducing macromolecular interactions with small molecules to activate cellular signaling is a
11 challenging goal. PROTACs (proteolysis-targeting chimaeras) are bifunctional molecules that
12 recruit a target protein in proximity to an E3 ubiquitin ligase to trigger protein degradation.
13 Structural elucidation of the key ternary species ligase:PROTAC:target and how this impacts
14 target degradation selectivity remains elusive. We solved the crystal structure of Brd4-
15 degrader MZ1 in complex with human VHL and the Brd4 bromodomain (Brd4^{BD2}). The
16 ligand folds into itself to allow formation of specific intermolecular interactions in the ternary
17 complex. Isothermal titration calorimetry studies, supported by surface mutagenesis and
18 proximity assays, are consistent with pronounced cooperative formation of ternary complexes
19 with Brd4^{BD2}. Structure-based designed compound AT1 exhibits highly selective depletion of
20 Brd4 in cells. Our results elucidate how PROTAC-induced *de novo* contacts dictate
21 preferential recruitment of a target protein into stable and cooperative complex with an E3
22 ligase for selective degradation.

23

24

25 Introduction

26 Regulating protein function through targeted degradation as opposed to more conventional
27 target inhibition has emerged as a new modality of discovery chemistry with attractive
28 potential both as tools for target validation and for the development of novel therapeutics¹⁻⁴.
29 PROTACs (proteolysis-targeting chimaeras) are bifunctional molecules that bring a target
30 protein into spatial proximity with an E3 ubiquitin ligase to trigger target ubiquitination and
31 subsequent proteasomal degradation⁵⁻¹¹. Recent developments in the field have led to
32 PROTACs being designed with increasingly “drug-like” molecular properties, and
33 remarkable activities both in cells and *in vivo*¹⁰. Furthermore, we and others have shown that
34 target depletion selectivity by PROTACs can significantly exceed the binding selectivity of
35 their constitutive warhead ligands^{7,12}. This realization provides proof-of-concept for turning
36 non-selective or promiscuous ligands into more selective degraders, which can be highly
37 desirable for both chemical probes and drug leads. A characteristic feature of PROTACs
38 mode of action is their sub-stoichiometric catalytic action that alleviates the requirement for
39 target engagement and occupancy of traditional inhibitors⁹. Effective redirection of a ligase
40 poly-ubiquitination activity toward a new substrate protein requires formation of a ternary
41 complex ligase:PROTAC:target, an intermediate species that is crucial to the cellular activity
42 of degrader molecules. However, structural elucidation of such ternary species and how it
43 may influence selectivity of target degradation remain elusive since the PROTAC concept
44 was first incepted and demonstrated in 2001 (ref.⁵).

45 In 2015 we and others reported the first examples of small-molecule PROTACs that target
46 the bromo- and extra-terminal (BET) family proteins for degradation by recruiting substrate-
47 recognition subunits von Hippel–Lindau protein (VHL)⁷ and cereblon (CRBN)^{6,8} of the
48 respective cullin RING ligases (CRLs), CRL2^{VHL} and CRL4^{CRBN}. Compound MZ1 (ref.⁷)
49 conjugates the pan-BET inhibitor JQ1 (ref.¹³) to VH032, a potent and specific VHL ligand
50^{14,15}, via a 3-unit PEG linker (**Fig. 1a**). MZ1 and its analogues, MZ2 and MZ3
51 (**Supplementary Results, Supplementary Fig. 1**), induce more effective depletion of a
52 single BET member, Brd4 (a validated drug target against cancer and other diseases¹⁶), over
53 its family paralogues Brd2 and Brd3 (ref.⁷). These observations led us to hypothesize a
54 structural basis for target selectivity, imparted as a result of PROTAC-induced recruitment of
55 the ligase and bromodomain together in a ternary complex. To reveal the molecular details of
56 complex formation, we pursued the crystal structure of MZ1 in complex with VHL and a
57 BET bromodomain. Here we present for the first time a structure of a PROTAC bound to
58 both E3 ligase and target protein. The structure reveals MZ1 is “sandwiched” between the
59 two proteins, inducing extensive new protein-protein and protein-ligand contacts of both
60 hydrophobic and electrostatic nature. Biophysical binding studies in solution allowed
61 measurement of full thermodynamics parameters of complex formation, which revealed
62 marked isoform-specific cooperativity of ternary complexes. Surface mutagenesis swap and
63 proximity binding assays data support the induced PPI contacts drive specificity of the
64 cooperative recognition, impacting on the relative population of ternary complexes.
65 Furthermore, new PROTAC molecules designed guided by the crystal structure showed
66 exquisite selectivity for inducing cellular depletion of Brd4 over its BET family members
67 Brd2 and Brd3.

68 Results

69 **Ternary complex crystal structure.** To elucidate the structural details of PROTAC-induced
70 substrate recruitment to an E3 ligase, we solved the crystal structure of MZ1 bound in a

71 ternary complex with the second bromodomain (BD) of Brd4 (Brd4^{BD2}) and VHL to 2.7 Å
72 resolution (**Fig. 1a, Supplementary Table 1**). The asymmetric unit of the crystal contained
73 two ternary Brd4^{BD2}:MZ1:VCB (VHL, ElonginB and ElonginC) complexes of overall
74 identical quaternary architecture (**Supplementary Fig. 2a**) and only minor deviations at
75 either end when superposed over the central VHL subunit (**Supplementary Fig. 2b,c**). The
76 first complex (chains A, B, C and D) had lower average *B* factors (**Supplementary Fig. 2a**)
77 so we refer to this in all subsequent analyses. The electron density around MZ1 was fully
78 defined (see inset panel in **Fig 1a** and **Supplementary Fig. 2d,e** for each protomer in the
79 asymmetric unit). MZ1 is bound within a bowl-shaped interface formed by extensive protein-
80 protein interactions (PPIs) between Brd4^{BD2} and VHL (**Supplementary Fig. 3a**). The bowl
81 has a hydrophobic "base" which is formed by two key points of contact (**Fig. 1b** and
82 **Supplementary Fig. 3a**). Firstly, Trp374 from the characteristic hydrophobic region named
83 "WPF shelf" (ref. ¹⁷) of Brd4^{BD2} interacts with residues Arg69, Pro71 and Tyr112 of VHL
84 (**Fig. 1b**). Pro71 provides an additional stack to the WPF, forming an extended "PWPF" shelf
85 (**Fig. 1b**). Secondly, Ala384 and Leu385 from the second helical turn of the ZA loop of
86 Brd4^{BD2} contact the hydrophobic side chains of Arg108, Ile109 and His110 in β4 of VHL
87 (**Fig. 1b**). Two electrostatic "arms" complete the rim of the bowl. At one end, Asp381 and
88 Glu383 in the ZA loop of Brd4^{BD2} form a tight zipper structure of complementary charges
89 with Arg107 and Arg108 (**Fig. 1c**). At the opposite end Brd4^{BD2} residue Glu438, residing in
90 the BC loop, contacts Arg69 from VHL (**Fig. 1d**). In the induced interface between the two
91 proteins, Brd4^{BD2} recapitulates some of the interactions made by the HIF-1α CODD segment
92 peptide with VHL ^{18,19}, as the electrostatic zipper structure generated by Asp381 and Glu383
93 contacts the same VHL residues (Arg107 and Arg108) as Asp569 and Asp571 of HIF-1α
94 (**Fig. 1c** and **Supplementary Fig. 3b,c**). In contrast, VHL does not contact the surface of
95 Brd4 bromodomain bound to acetyllysine histone H4 peptide ²⁰ (**Supplementary Fig. 3d,e**).
96 In total the PPIs induced in the complex bury a surface area of 688 Å² (**Supplementary**
97 **Table 2**).

98 MZ1 is cupped within the bowl structure in such a way that its two heads recapitulate the
99 binding modes of the respective ligands individually – JQ1 in the acetyllysine-binding pocket
100 of Brd4^{BD2} ^{13,20}, and VH032 in the hydroxyproline-binding site of VHL ¹⁴ (**Supplementary**
101 **Fig. 3f,g**). In addition to the expected binary protein-ligand interactions, MZ1 forms
102 additional protein-ligand interactions within the ternary complex. The PEG linker makes van
103 der Waals interactions with the BC loop of Brd4^{BD2} and a hydrogen bond between the ether
104 oxygen adjacent to the amide linkage to JQ1 and the BD2-specific residue His437 (**Fig. 1d**).
105 The same hydrogen bond between His437 and a PEG oxygen is also observed in a recent
106 crystal structure of Brd4^{BD2} bound to MT1, a bivalent BET inhibitor comprised of two JQ1
107 moieties linked by a PEG unit in a similar fashion as in MZ1 (**Supplementary Fig. 4**) ²¹.
108 VHL and Brd4^{BD2} come together to sandwich MZ1 against their respective binding surfaces,
109 burying otherwise solvent-exposed regions of the JQ1 and VH032 ligands. Specifically,
110 Ala384, Leu385 and Gly386 from the ZA loop of Brd4^{BD2} contact the –CH₂–phenyl portion
111 of VH032, whilst His110 and Tyr112 of β4 of VHL contact one of the two thiophene methyl
112 groups and the *para*-chlorophenyl ring of JQ1 (**Fig. 1b**). In addition, MZ1 folds onto itself in
113 such a way that its PEG linker is packed between the *tert*-butyl group of the VH032 moiety
114 and the *para*-chlorophenyl ring of JQ1 (**Fig. 1a,d**). Throughout a 100 ns molecular dynamics
115 simulation, favorable intermolecular contacts were observed from JQ1 atoms to VHL, from
116 VH032 atoms to Brd4^{BD2}, and from the PEG linker atoms to both VHL and Brd4^{BD2}, as well
117 as intramolecular contacts within MZ1 involving the PEG linker and the JQ1 and VH032
118 moieties (**Fig. 2a** and **Supplementary Fig. 5**). The surface area further buried by the ligand
119 folding within the bowl-shaped interface was 1,933 Å², resulting in a total extended buried

120 surface area of 2,621 Å² for the ternary complex (see **Supplementary Table 2** for a
121 comparison with cereblon:phthalimides:target ternary complexes^{2,3}).

122 **Isoform-specific cooperativity of ternary complexes.** The extensive new contacts observed
123 in the crystal structures suggested the possibility that isoform-specific PPIs could play a role
124 in the “cooperativity” of the ternary complex equilibria^{22,23}. To assess the thermodynamics of
125 PROTAC-induced complex formation with VHL and BET BDs, we employed isothermal
126 titration calorimetry (ITC) in solution (**Table 1** and **Supplementary Fig. 6**). To disentangle
127 contributions from binary and ternary complex formation equilibria we performed reverse
128 titrations i.e. protein in syringe and ligand in cell. This experimental strategy avoids the
129 characteristic “hook effect” observed with increasing concentrations of PROTACs, as
130 formation of binary complexes competes with and eventually surpasses formation of ternary
131 ones²³. First, we titrated a solution of BET BD against MZ1, ensuring no excess unbound
132 PROTAC compound would be present at the end of the titration. This was followed by a
133 titration of VCB into the saturated MZ1:BD complex, forming the ternary VCB:MZ1:BD
134 complex (**Fig. 2b**, right panel). Titration of VCB into MZ1 alone (**Fig. 2b**, left panel) was
135 then performed and used as reference, allowing potential cooperativity of ternary complex
136 formation to be accurately quantified. By definition, a ternary system is considered *positively*
137 cooperative if interactions enhance formation of the ternary complex ($\alpha = \frac{K_d(\text{Binary})}{K_d(\text{Ternary})} > 1$;
138 $\Delta pK_d = pK_d^T(\text{ternary}) - pK_d(\text{binary}) > 0$). Conversely, a system is termed *negatively*
139 cooperative when formation of the ternary complex is diminished ($\alpha < 1$; $\Delta pK_d < 0$), for
140 example because of repulsive interactions or steric hindrance between the two components in
141 the ternary complex. Non-cooperative equilibria would instead show unchanged K_d for the
142 two steps ($\alpha = 1$; $\Delta pK_d = 0$), suggesting no interactions (**Fig. 2c**). With all BET BDs used, we
143 observed significant positively cooperative ternary complex formation (see **Table 1**, and plots
144 of ΔpK_d in **Fig. 2d**). Strikingly, the strongest cooperativity was observed for Brd4^{BD2} ($\alpha =$
145 18), followed by Brd3^{BD2} ($\alpha = 11$; **Table 1** and **Fig. 2d**). The large cooperativity observed led
146 to steep transition of the sigmoidal binding curve (**Fig. 2b**, right panel), suggesting that the
147 fitted K_d value could potentially be underestimating the real binding affinity of this ternary
148 complex. All BD1s also exhibited positive cooperativity, albeit to a much lesser extent (α
149 between 2 and 3). Brd4^{BD2} and Brd3^{BD2} not only exhibited the greatest cooperativity amongst
150 all BET BDs, they also formed the most stable ternary complexes overall ($\Delta G(\text{binary} +$
151 $\text{ternary}) = -22.2 \pm 0.1$ and 22.0 ± 0.2 kcal/mol, respectively), ~2 kcal/mol more stable than
152 e.g. Brd2^{BD1} ($\Delta G = -20.3 \pm 0.2$ kcal/mol).

153 To understand the impact of cooperativities of different BET BDs ternary complexes on their
154 relative population, we applied a mathematical model of ternary equilibrium²³. We simulated
155 the fraction of ternary complex formation for VCB, MZ1 and six individual BET BDs, using
156 our measured binary K_{dS} and cooperativities α (**Table 1**) and protein concentrations of 40 nM
157 (to be around the K_d values and to match the concentrations used later in AlphaLISA).
158 Overlay of simulations showed that the relative populations of each ternary complex vary
159 significantly, with Brd4^{BD2} being the most populated, and, as an example, ~2.5 fold greater
160 than Brd2^{BD1} at any given concentration of PROTAC (**Fig. 2e**). To interrogate this relative
161 trend experimentally, we employed a proximity AlphaLISA assay that can achieve high
162 signal amplification in response to formation of ternary complexes over an energy transfer
163 distance of up to 200 nm^{24,25}. At every fixed component concentration, the relative trend
164 observed in AlphaLISA signal was broadly consistent with the cooperativity trends measured
165 by ITC, with Brd4^{BD2} and Brd3^{BD2} giving greater signal, while Brd2^{BD1} giving the lowest
166 response (**Fig. 2f**). A similar trend was observed with the analogous MZ2 (PEG₄), MZ3

167 (PEG₃-Phe) and MZ4 (PEG₂) (**Supplementary Fig. 7a–h**). Taken together the data are
168 consistent with target-specific cooperativities and stabilities of ternary complexes impacting
169 on the relative population of this key intermediate species.

170 **Specificity of MZ1-induced protein-protein interactions.** To evaluate to what extent the
171 cooperativity of ternary complex formation is dictated by surface complementarity between
172 VHL and the Brd4^{BD2} bromodomain, we mutated semi-conserved or non-conserved
173 bromodomain residues forming key induced PPI contacts, but not directly involved in
174 binding of MZ1 (**Fig. 3a** and **Supplementary Fig. 5**). Inspection of sequence alignments
175 (**Fig. 3a**) and the crystal structure (**Fig. 3b**) guided us to select residues Glu383 and Ala384 in
176 Brd4^{BD2} (the most cooperative of bromodomains), for site directed mutagenesis. These
177 residues are Val106 and Lys107 in the corresponding positions in Brd2^{BD1}, one of the least
178 cooperative BET domains. In addition, the MD simulation evidenced extensive movement of
179 loop 7 of VHL (ref. ²⁶) bringing it in close contact with Lys378 of Brd4^{BD2} (**Supplementary**
180 **Fig. 5b–d**), which corresponds to Gln101 in Brd2^{BD1}. Based on these considerations, triple
181 mutant Brd4^{BD2} K378Q/E383V/A384K (named QVK for simplicity) was designed. The
182 mutations would make the PPI surface of Brd4^{BD2} closer to that of Brd2^{BD1}, albeit with the
183 caveat of introducing an extra charge overall. Conversely, a triple mutant of Brd2^{BD1} was
184 designed in which the corresponding residues are switched to those of Brd4^{BD2}
185 (Q101K/V106E/K107A, named KEA for simplicity). In ITC, the QVK mutant exhibited
186 significantly weakened cooperative complex formation relative to Brd4^{BD2} wild-type (WT) (α
187 = 4; **Table 1** and $\Delta pK_d = 0.64 \pm 0.04$, see plots in **Fig. 3c**). Conversely, the cooperativity of
188 the KEA mutant increased relative to Brd2^{BD1} WT ($\alpha = 8$; **Table 1** and **Fig. 3c**). Crucially,
189 these mutations did not affect the K_d of each domain for MZ1 (**Table 1**), suggesting that the
190 switch of cooperativity is independent of binary target engagement and instead is dictated by
191 the induced PPIs. Consistent with the cooperativity switch measured by ITC, QVK reduced
192 ternary complex formation in AlphaLISA compared to WT, whereas KEA displayed the
193 opposite effect (**Fig. 3d** with MZ1 and **Supplementary Fig. 7i** with MZ2). Taken together
194 these data validate the ternary complex structure in solution and elucidate how specific PPIs
195 influence cooperative recruitment of two target proteins to each other by a bifunctional
196 molecule.

197 **Structure-designed AT1 is highly selective Brd4 degrader.** In chemical probe and drug
198 development knowledge of ligand-bound structures can guide the design of next-generation
199 compounds. We therefore sought to create new PROTACs based on our crystal structure that
200 could exhibit enhanced target depletion selectivity in cells toward Brd4. We noted that the
201 side chain of the key *tert*-Leu group of VH032 projected an attractive vector to link directly
202 to the JQ1 moiety (**Fig. 4a**), which we hypothesized could better discriminate against the
203 relative binding orientation observed in the crystal. We therefore replaced *tert*-Leu with
204 penicillamine and synthesized **1** (AT1, **Fig. 4b**) and other analogues **2–6** (AT2–AT6) bearing
205 thioether linkages of varying length to JQ1 (**Supplementary Fig. 1** and **Methods**). The
206 modified VHL ligand within AT1 retained binding to VHL (K_d 330 nM, **Supplementary**
207 **Table 3**, and **Supplementary Fig. 8**), a less than two-fold loss of potency relative to VH032
208 (ref. ¹⁴) but approximately five-fold less compared to MZ1. ITC data comparing binary and
209 ternary complexes revealed Brd4^{BD2} as the BET bromodomain forming the most cooperative
210 ($\alpha = 7$; $\Delta pK_d = 0.84 \pm 0.07$) and most stable ($\Delta G = -20.2 \pm 0.2$ kcal/mol) of all ternary
211 complexes with AT1 (**Fig. 4c**, **Supplementary Table 3**, and **Supplementary Fig. 8**). The
212 same trend of cooperativity observed for MZ1 and the QVK and KEA mutants relative to WT
213 was also observed with AT1 (**Fig. 4c**, **Supplementary Table 3**), suggesting AT1 recruits
214 VHL and Brd4^{BD2} in the same relative orientation as does MZ1. We consistently observed by

215 AlphaLISA preferential recruitment of Brd4^{BD2} over the other BDs by AT1–6 (**Fig. 4d** and
216 **Supplementary Fig. 9**). We next tested the activity of the new structure-designed molecules
217 to induce degradation of BET proteins in cells, and observed remarkable Brd4-selective
218 depletion at all concentrations tested, with depletion of Brd4 after 24 h treatment with 1–3
219 μM of AT1 and negligible activity against Brd2 and Brd3 (**Fig. 4e**, see **Supplementary Fig.**
220 **9** for AT2–6). Specificity for Brd4 degradation was not due to differences in protein synthesis
221 rates, as shown by control treatments with cycloheximide, which blocks protein translation
222 (**Supplementary Fig. 10**). To assess whether ubiquitination of lysine residues could play a
223 role in the observed selectivity, we combined our EloBC–VHL–MZ1–Brd4^{BD2} complex with
224 existing whole CRL structural information into a model of the entire CRL2^{VHL}–MZ1–
225 bromodomain assembly (**Supplementary Fig. 12a**). Several lysine residues are surface
226 exposed and accessible to the E2-Ub in this model at distances between 50–60 Å, consistent
227 with known CRL substrates²⁷. Mapping MZ1-induced ubiquitination sites *in vitro* identified
228 Lys346 on Brd4^{BD2} and several sites on the other BET-BDs (**Supplementary Fig. 12b-d**).
229 Unbiased and quantitative isobaric tagging mass spectrometry proteomics confirmed Brd4 as
230 the sole protein markedly depleted (to ~40%) upon treatment with AT1, amongst the 5,674
231 detected proteins that passed filtering criteria (**Fig. 4f** and **Supplementary Data Set 1**).
232 Crucially, no effect on protein levels of Brd2 and Brd3 was observed with AT1, in contrast
233 with MZ1 that exerted a broader and more profound effect across all BET proteins, albeit still
234 preferential toward Brd4 (**Fig. 4g**). Together these data qualify AT1 as a new highly selective
235 degrader of Brd4 in cells.

236 Discussion

237 We put forth a model for how cooperative recruitment of a target close to an E3 ligase in a
238 ternary complex by a PROTAC molecule can impact on the effectiveness and selectivity of
239 target degradation (**Fig. 5**). Our work shines structural insights into how bifunctional
240 molecules can induce target-specific interactions in the ‘enzyme-substrate’ ternary complex
241 species key for PROTAC catalytic activity. These cooperative molecular recognition features
242 contribute to how tightly and stably the ‘*neo*-substrate’ can be bound to the ligase, impacting
243 on the relative population of the complex and consequently on the catalytic efficiency of the
244 process. For homologous targets as is the case with BET bromodomains, we show how these
245 features add a level of target depletion selectivity independently of binary target engagement.

246 We illustrate the relevance of measuring cooperativities of ternary complex formation in
247 solution using ITC. One of the main advantages of the assay set-up as described here is that it
248 is designed to avoid issues associated with the hook effect. While the assay may be used to
249 characterize in full a handful of compounds and systems, it requires large quantities of
250 material and notably lacks throughput. Alternative bioassays to quantify formation of ternary
251 complexes could circumvent this limitation, and we provide evidence that proximity
252 AlphaLISA assay can be used for these purposes. However, AlphaLISA data should be
253 interpreted with caution, even when comparing highly conserved domains as done here,
254 because in this bead-based technology the multiplicity of binding sites and relative linkage
255 and orientation of components immobilized to the beads may influence the measured signal
256^{24,28}. Moreover, it can be difficult to deconvolute individual binding parameters from dose–
257 response curves monitoring ternary complex formation, because these are often bell-shaped
258 curves complicated by the hook effect²³. We anticipate that future assay developments in this
259 direction will help prioritize complexes for structural studies and to drive drug development
260 programs. The results of our study are of particular relevance because VHL-based BET

261 degraders similar to the ones described here have proven to be bioavailable and active *in vivo*
262 ²⁹ and could potentially enter clinical trials as early as 2017 (ref. ⁴).

263 Our study points to the importance that the bifunctional molecule “folds in itself” in such a
264 way that its two heads can recruit the respective targets into productive proximity. The result
265 of this process is the burial of extensive surface area, the formation of new PPIs, contributing
266 to the high stability and cooperativity of ternary complexes. Our work has therefore major
267 implications for future PROTAC drug design, which has so far been somewhat empirical and
268 has largely adopted a combinatorial “plug-and-play” strategy ¹¹. The proposed model
269 suggests that bifunctional molecules should be rationally designed and prioritized based on
270 their ability to induce favorable contacts and allow forming a stable complex between the E3
271 ligase and the target. While ligand-induced proximity is expected to strengthen potential PPIs
272 because of the reduced entropic cost, we show that the level of surface complementarity
273 between the two proteins in their relative orientation imposed by the bifunctional molecule
274 dictates cooperative complexation. While the exact relative orientation between VHL and
275 Brd4 observed in the crystal may not be the only one that the system can adopt in solution
276 once free from potential constraints of crystal packing, our data suggests that it captures a
277 significant species underlying MZ1 function. Maximizing the diversity of E3s recruited ³⁰,
278 and linking positions and vectors from the E3 and target ligands, will thus be important to
279 achieve target-specific degraders.

280 In an example of first layer of this rational design, we show how new PROTACs designed
281 based on our ternary structure can lead to enhanced selectivity of depletion in cells for the
282 crystallized target Brd4. The efficiency and selectivity of cellular protein knockdown will
283 inevitably depend on other factors, including compound permeability and stability, the
284 expression level of the hijacked CRL and its relative activity and flexibility ^{27,31}, as well as
285 target abundance and re-synthesis rates. Differing ubiquitination rates could also in principle
286 influence target degradation selectivity. To this end, in addition to increasing their relative
287 population, cooperative and stable complexes would be expected to exhibit slower
288 dissociation rates and longer half-lives, potentially aiding the efficiency of target
289 ubiquitination by the hijacked ligase. Differing availability and access of surface lysine
290 residues between alternate substrates could also play a role. However, based on our data, the
291 presence of many surface Lys on BET-BDs, and the flexibility and large ubiquitination zone
292 of CRLs ^{2,27}, we view it unlikely that target ubiquitination plays a role in the observed
293 selectivity of Brd4 degradation. Obtaining a more detailed biochemical picture of target
294 ubiquitination in a cellular context will be of clear importance for future investigation.

295 For targeted protein degradation, converting a pan-selective or promiscuous probe ligand into
296 a more selective degrader probe provides new opportunities to improve target validation and
297 could minimize off-target effects. In addition to dictate selectivity of target degradation,
298 highly cooperative ternary E3:PROTAC:target systems would be anticipated to unlock the
299 possibility to effectively degrade hitherto “undruggable” targets using ligands with inherently
300 weak binary binding affinities. A more general implication of this study is the feasibility to
301 induce *de novo* protein-protein interactions, or stabilize weakened ones, using bifunctional
302 small molecules, a feature previously established with mono-functional ‘molecular glues’ ³²
303 such as the plant hormones auxin ³³ and jasmonate ³⁴, the phthalimide immunomodulatory
304 drugs (IMiDs) ^{2,3,31,35-38}, and macrocyclic natural products such as rapamycin and
305 cyclosporine ^{39,40}. We envision that extensions of PPI-stabilizing capabilities to hetero- or
306 homo-bifunctional small molecules ^{21,41,42} beyond PROTACs as highlighted here could

307 expand the target spectrum accessible to PPI stabilizers, and provide a new paradigm of
308 selective chemical intervention for structural chemical biology and drug discovery.

309

310 **METHODS**

311 Methods and any associated references are available in the online version of the paper.

312 **Accession codes**

313 Atomic coordinates and structure factors for hsBrd4^{BD2}-MZ1-hsVHL-hsEloC-hsEloB have
314 been deposited in the Protein Data Bank (PDB) under accession number 5T35.

315

316 **Data availability**

317 Any supplementary information, chemical compound information and source data are
318 available in the online version of the paper. Correspondence and requests for materials should
319 be addressed to A.C. (a.ciulli@dundee.ac.uk).

320

321 **Acknowledgements**

322 This work was supported by the European Research Council (ERC-2012-StG-311460
323 DrugE3CRLs Starting Grant to A.C.); the UK Biotechnology and Biological Sciences
324 Research Council (BBSRC grant BB/J001201/2 to A.C.); the European Commission (H2020-
325 MSCA-IF-2014-655516 Marie Skłodowska-Curie Actions Individual Fellowship to K.-H.C.,
326 and H2020-MSCA-IF-2015-806323 Marie Skłodowska-Curie Actions Individual Fellowship
327 to X.L.); and the Wellcome Trust (Strategic Awards 100476/Z/12/Z for biophysics and drug
328 discovery and 094090/Z/10/Z for structural biology and X-ray crystallography to the Division
329 of Biological Chemistry and Drug Discovery). We are thankful to P. Fyfe for support with
330 the in-house X-ray facility; L. Finn for support with tissue culture facility (MRC-PPU); the
331 Ferguson lab for access to LI-COR equipment; T. Cardote for the gift of full-length Cul2-
332 Rbx1 and A. Knebel (MRC-PPU/DSTT) for the gift of E1 and E2 enzymes; the Division of
333 Computational Biology for support with computational cluster; and to Diamond Light Source
334 for beamtime (BAG proposal MX10071) and beamline support at beamline I04-1.

335

336 **Author Contributions**

337 A.C. conceived the idea and directed the project.
338 M.S.G., X.L., A.T., K.-H.C. and A.C. designed the experiments and interpreted results
339 M.S.G., X.L., A.T., and K.-H.C. performed experiments
340 A.T. and M.Z. contributed to compound design and synthesized compounds
341 W.C. performed MS proteomics experiments under the supervision of D.J.L.
342 M.S.G., X.L. and A.C. wrote the manuscript with input from all other authors.

343

344 **Competing financial interests**

345 The authors declare no competing financial interests.

346

347 **References**

- 348 1. Huang, X. & Dixit, V. M. Drugging the undruggables: exploring the ubiquitin system
349 for drug development. *Cell Res* **26**, 484–498 (2016).
- 350 2. Petzold, G., Fischer, E. S. & Thomä, N. H. Structural basis of lenalidomide-induced

- 351 CK1 α degradation by the CRL4(CRBN) ubiquitin ligase. *Nature* **532**, 127–130 (2016).
- 352 3. Matyskiela, M. E. *et al.* A novel cereblon modulator recruits GSPT1 to the
353 CRL4(CRBN) ubiquitin ligase. *Nature* **535**, 252–257 (2016).
- 354 4. Lai, A. C. & Crews, C. M. Induced protein degradation: an emerging drug discovery
355 paradigm. *Nat Rev Drug Discov* (2016). doi:10.1038/nrd.2016.211
- 356 5. Sakamoto, K. M. *et al.* Protacs: chimeric molecules that target proteins to the Skp1-
357 Cullin-F box complex for ubiquitination and degradation. *P Natl Acad Sci Usa* **98**,
358 8554–8559 (2001).
- 359 6. Winter, G. E. *et al.* Phthalimide conjugation as a strategy for in vivo target protein
360 degradation. *Science* **348**, 1376–1381 (2015).
- 361 7. Zengerle, M., Chan, K.-H. & Ciulli, A. Selective Small Molecule Induced Degradation
362 of the BET Bromodomain Protein BRD4. *ACS Chem Biol* **10**, 1770–1777 (2015).
- 363 8. Lu, J. *et al.* Hijacking the E3 Ubiquitin Ligase Cereblon to Efficiently Target BRD4.
364 *Chem Biol* **22**, 755–763 (2015).
- 365 9. Bondeson, D. P. *et al.* Catalytic in vivo protein knockdown by small-molecule
366 PROTACs. *Nat Chem Biol* **11**, 611–617 (2015).
- 367 10. Deshaies, R. J. Protein degradation: Prime time for PROTACs. *Nat Chem Biol* **11**,
368 634–635 (2015).
- 369 11. Toure, M. & Crews, C. M. Small-Molecule PROTACS: New Approaches to Protein
370 Degradation. *Angew Chem Int Ed Engl* **55**, 1966–1973 (2016).
- 371 12. Lai, A. C. *et al.* Modular PROTAC Design for the Degradation of Oncogenic BCR-
372 ABL. *Angew Chem Int Ed Engl* **55**, 807–810 (2016).
- 373 13. Filippakopoulos, P. *et al.* Selective inhibition of BET bromodomains. *Nature* **468**,
374 1067–1073 (2010).
- 375 14. Galdeano, C. *et al.* Structure-guided design and optimization of small molecules
376 targeting the protein-protein interaction between the von Hippel-Lindau (VHL) E3
377 ubiquitin ligase and the hypoxia inducible factor (HIF) alpha subunit with in vitro
378 nanomolar affinities. *J Med Chem* **57**, 8657–8663 (2014).
- 379 15. Frost, J. *et al.* Potent and selective chemical probe of hypoxic signalling downstream
380 of HIF- α hydroxylation via VHL inhibition. *Nat Commun* **7**, 13312 (2016).
- 381 16. Zuber, J. *et al.* RNAi screen identifies Brd4 as a therapeutic target in acute myeloid
382 leukaemia. *Nature* **478**, 524–528 (2011).
- 383 17. Nicodeme, E. *et al.* Suppression of inflammation by a synthetic histone mimic. *Nature*
384 **468**, 1119–1123 (2010).
- 385 18. Hon, W.-C. *et al.* Structural basis for the recognition of hydroxyproline in HIF-1 alpha
386 by pVHL. *Nature* **417**, 975–978 (2002).
- 387 19. Min, J.-H. *et al.* Structure of an HIF-1alpha -pVHL complex: hydroxyproline
388 recognition in signaling. *Science* **296**, 1886–1889 (2002).
- 389 20. Filippakopoulos, P. *et al.* Histone recognition and large-scale structural analysis of the
390 human bromodomain family. *Cell* **149**, 214–231 (2012).
- 391 21. Tanaka, M. *et al.* Design and characterization of bivalent BET inhibitors. *Nat Chem*
392 *Biol* **12**, 1089–1096 (2016).
- 393 22. Whitty, A. Cooperativity and biological complexity. *Nat Chem Biol* **4**, 435–439
394 (2008).
- 395 23. Douglass, E. F., Miller, C. J., Sparer, G., Shapiro, H. & Spiegel, D. A. A
396 comprehensive mathematical model for three-body binding equilibria. *J Am Chem Soc*
397 **135**, 6092–6099 (2013).
- 398 24. Eglén, R. M. *et al.* The use of AlphaScreen technology in HTS: current status. *Curr*
399 *Chem Genomics* **1**, 2–10 (2008).
- 400 25. Roberts, J. M. & Bradner, J. E. A Bead-Based Proximity Assay for BRD4 Ligand

- 401 Discovery. *Curr Protoc Chem Biol* **7**, 263–278 (2015).
- 402 26. Stebbins, C. E., Kaelin, W. G. & Pavletich, N. P. Structure of the VHL-ElonginC-
403 ElonginB complex: implications for VHL tumor suppressor function. *Science* **284**,
404 455–461 (1999).
- 405 27. Duda, D. M. *et al.* Structural insights into NEDD8 activation of cullin-RING ligases:
406 conformational control of conjugation. *Cell* **134**, 995–1006 (2008).
- 407 28. Zhou, M., Li, Q. & Wang, R. Current Experimental Methods for Characterizing
408 Protein-Protein Interactions. *ChemMedChem* **11**, 738–756 (2016).
- 409 29. Raina, K. *et al.* PROTAC-induced BET protein degradation as a therapy for castration-
410 resistant prostate cancer. *P Natl Acad Sci Usa* **113**, 7124–7129 (2016).
- 411 30. Bulatov, E. & Ciulli, A. Targeting Cullin-RING E3 ubiquitin ligases for drug
412 discovery: structure, assembly and small-molecule modulation. *Biochem J* **467**, 365–
413 386 (2015).
- 414 31. Fischer, E. S. *et al.* Structure of the DDB1-CRBN E3 ubiquitin ligase in complex with
415 thalidomide. *Nature* **512**, 49–53 (2014).
- 416 32. Fischer, E. S., Park, E., Eck, M. J. & Thomä, N. H. SPLINTS: small-molecule protein
417 ligand interface stabilizers. *Curr Opin Struct Biol* **37**, 115–122 (2016).
- 418 33. Tan, X. *et al.* Mechanism of auxin perception by the TIR1 ubiquitin ligase. *Nature*
419 **446**, 640–645 (2007).
- 420 34. Sheard, L. B. *et al.* Jasmonate perception by inositol-phosphate-potentiated COI1-JAZ
421 co-receptor. *Nature* **468**, 400–405 (2010).
- 422 35. Ito, T. *et al.* Identification of a primary target of thalidomide teratogenicity. *Science*
423 **327**, 1345–1350 (2010).
- 424 36. Lu, G. *et al.* The myeloma drug lenalidomide promotes the cereblon-dependent
425 destruction of Ikaros proteins. *Science* **343**, 305–309 (2014).
- 426 37. Krönke, J. *et al.* Lenalidomide causes selective degradation of IKZF1 and IKZF3 in
427 multiple myeloma cells. *Science* **343**, 301–305 (2014).
- 428 38. Chamberlain, P. P. *et al.* Structure of the human Cereblon-DDB1-lenalidomide
429 complex reveals basis for responsiveness to thalidomide analogs. *Nat Struct Mol Biol*
430 **21**, 803–809 (2014).
- 431 39. Pommier, Y. & Marchand, C. Interfacial inhibitors: targeting macromolecular
432 complexes. *Nat Rev Drug Discov* **11**, 25–36 (2012).
- 433 40. Thiel, P., Kaiser, M. & Ottmann, C. Small-Molecule Stabilization of Protein-Protein
434 Interactions: An Underestimated Concept in Drug Discovery? *Angew Chem Int Ed*
435 *Engl* **51**, 2012–2018 (2012).
- 436 41. Illendula, A. *et al.* A small-molecule inhibitor of the aberrant transcription factor
437 CBF β -SMMHC delays leukemia in mice. *Science* **347**, 779–784 (2015).
- 438 42. Waring, M. J. *et al.* Potent and selective bivalent inhibitors of BET bromodomains.
439 *Nat Chem Biol* **12**, 1097–1104 (2016).
- 440

441 Figure Legends

442 **Figure 1. The crystal structure of the Brd4^{BD2}:MZ1:VHL-ElonginC-ElonginB complex. a,**
443 Overall structure of Brd4^{BD2}:MZ1:VHL-ElonginC-ElonginB in ribbon representation. Top middle,
444 chemical structure of bifunctional PROTAC molecule MZ1. Top right, $F_o - F_c$ omit map generated
445 prior to ligand modelling contoured at 3.0σ around bound MZ1. **b,** Key residues forming the
446 hydrophobic "base" of the induced Brd4^{BD2}:VHL interface. The "WPF" shelf of Brd4^{BD2} and extended
447 "PWPF" stack are outlined in black. The JQ1 and VH032 elements of MZ1 are labelled in yellow. **c,**
448 Electrostatic potential map showing the charged zipper contacts between Brd4^{BD2} residues D381 and
449 E383 with VHL residues R107 and R108. **d,** Electrostatic potential map showing the interaction

450 between Brd4^{BD2} residue E438 with VHL residue R69. The hydrogen bond between H437 of Brd4^{BD2}
451 and the PEG linker of MZ1 is also shown. Dashed lines indicate hydrogen bonds with shown distance
452 in angstroms (Å).

453

454 **Figure 2. Brd4^{BD2} and VHL form a stable, cooperative complex in the presence of MZ1.** **a**, Novel
455 ligand contacts are induced by ternary complex formation. Colour strength (from white to red)
456 indicates the mean enthalpic energies of individual MZ1 atoms in contacting Brd4^{BD2} (left) or VHL
457 (right), as well as intra-ligand contacts within MZ1 (centre) in a 100 ns MD simulation. **b**, Inverse
458 ITC titrations of VCB into MZ1 (left, representative of eight replicates) and VCB into the pre-formed
459 MZ1:Brd4^{BD2} (right, performed in duplicate) **c**, Ternary complex equilibria and definition of
460 cooperativities. **d**, ΔpK_d measured for VCB with MZ1 and the indicated BET-BDs, reported as
461 difference (\pm uncertainty), from pK_d values measured as mean (\pm 1 s.e.m.) as described in Online
462 Methods. Statistical significance of pK_d values for ternary titrations compared to the corresponding
463 binary titrations was assessed by two-tailed *t*-test assuming equal variances, and is indicated as * (*p*-
464 value < 0.05), ** (*p*-value < 0.01) or *** (*p*-value < 0.001). **e**, Simulated fraction of ternary
465 complexes based on mathematical model described in ref. ²³. **f**, AlphaLISA intensity values titrating
466 VCB against BET-BDs with MZ1. AlphaLISA intensities represent mean (\pm 1 s.d.) of intensity values
467 from four technical replicates. The hook effect observed on these curves is due to biotinylated-VCB
468 oversaturating the donor beads, resulting in a progressive decrease in signal.

469

470 **Figure 3. The molecular basis of MZ1-induced compact complex formation between Brd4^{BD2}**
471 **and VHL.** **a**, Sequence alignment of BET bromodomains. Residues of Brd4^{BD2} in contact with MZ1
472 and/or VHL are highlighted. **b**, Structural alignment of Brd2^{BD1} (yellow) superposed on Brd4^{BD2} (dark
473 green) in the ternary structure with MZ1 and VHL. Key, non-conserved interacting residues are
474 shown in sticks. **c**, ΔpK_d measured for VCB with MZ1 and the indicated BET-BDs, reported as
475 difference (\pm uncertainty), from pK_d values measured as mean (\pm 1 s.e.m.) as described in Online
476 Methods. Statistical significance of pK_d values for ternary titrations compared to the corresponding
477 binary titrations (in black) and for ternary titrations of WT compared to the corresponding triple-
478 mutant (in red) was assessed by two-tailed *t*-test assuming equal variances, and is indicated as * (*p*-
479 value < 0.05), ** (*p*-value < 0.01) or *** (*p*-value < 0.001). **d**, AlphaLISA intensity values titrating
480 Brd2^{BD1}, Brd4^{BD2} and corresponding mutants against VCB with MZ1. AlphaLISA intensities are the
481 mean (\pm 1 s.d.) of intensity values from four technical replicates.

482

483 **Figure 4. Structure-guided design and characterization of Brd4-selective degrader AT1.** **a**, A
484 vector linking VH032 to JQ1 that maintains the relative binding orientation. **b**, Chemical structure of
485 AT1. **c**, ΔpK_d measured for VCB with AT1 and the indicated BET-BDs, reported as difference (\pm
486 uncertainty), from pK_d values measured as mean (\pm 1 s.e.m.). Statistical significance of pK_d values for
487 ternary titrations compared to corresponding binary (black) and for ternary WT compared to
488 corresponding mutant (red) was assessed by two-tailed *t*-test assuming equal variances. **d**, AlphaLISA
489 intensity values titrating VCB against BET-BDs with AT1 (left) and BET-BDs against VCB with
490 AT1 (right). AlphaLISA intensities are the mean (\pm 1 s.d.) of intensity values from four technical
491 replicates. **e–g**, Highly selective degradation of Brd4 by AT1 in HeLa cells after 24 h. **e**, Protein levels
492 are shown from one representative of three biological replicates, visualized by immunoblot (left) and
493 quantified relative to DMSO (right). Intensity values were measured as described in Online Methods.
494 Full gels are provided in Supplementary Fig. 11. **f**, Impact of AT1 (1 μ M, 24 h) on the cellular
495 proteome. Data plotted as fold change (\log_2) of replicate 1 vs replicate 2, for a total of 5,674 proteins
496 quantified (see Online Methods). **g**, Quantified levels of BET proteins shown are mean (\pm 1 s.e.m.)

497 from two replicates relative to mean of vehicle. Statistical significance of relative protein abundance
498 compared to DMSO was assessed by two-tailed *t*-test assuming equal variances. Statistical
499 significance indicated as * (*p*-value < 0.05), ** (*p*-value < 0.01) or *** (*p*-value < 0.001).

500

501 **Figure 5. Schematic model of selective PROTAC-induced target degradation.** A target is
502 preferentially recruited in a stable and positively cooperative ternary complex with the E3 ubiquitin
503 ligase upon folding of the bifunctional probe to induce formation of specific PPIs.

504

505

506 **Table 1. Thermodynamic parameters of formation of binary and ternary complexes between MZ1, VCB and BET**
 507 **bromodomains measured by isothermal titration calorimetry.**

Protein in syringe	Species in cell	K_d (nM)	ΔG (kcal \times mol ⁻¹)	ΔH (kcal \times mol ⁻¹)	$-T\Delta S$ (kcal \times mol ⁻¹)	N	α	ΔpK_d
Brd2 ^{BD1}	MZ1	62 \pm 6	-9.84 \pm 0.06	-12.8 \pm 0.7	3.0 \pm 0.8	1.1 \pm 0.1		
Brd2 ^{BD2}		60 \pm 3	-9.85 \pm 0.03	-9.8 \pm 0.3	-0.1 \pm 0.3	1.2 \pm 0.1		
Brd3 ^{BD1}		21 \pm 5	-10.2 \pm 0.1	-14.7 \pm 0.8	4.2 \pm 0.9	1.1 \pm 0.1		
Brd3 ^{BD2}		13 \pm 3	-10.8 \pm 0.1	-14.0 \pm 0.9	3.3 \pm 0.7	1.05 \pm 0.02		
Brd4 ^{BD1}		39 \pm 9	-10.1 \pm 0.1	-14.7 \pm 0.4	4.6 \pm 0.5	0.95 \pm 0.03		
Brd4 ^{BD2}		15 \pm 1	-10.68 \pm 0.04	-10.9 \pm 0.4	0.2 \pm 0.4	1.08 \pm 0.07		
Brd2 ^{BD1} KEA		69 \pm 9	-9.78 \pm 0.08	-14 \pm 1	4 \pm 1	0.83 \pm 0.08		
Brd4 ^{BD2} QVK		22 \pm 8	-10.5 \pm 0.2	-12.4 \pm 0.5	1.9 \pm 0.2	1.0 \pm 0.1		
VCB ^a	MZ1 ^a	66 \pm 6	-9.81 \pm 0.05	-7.7 \pm 0.3	-2.1 \pm 0.3	0.93 \pm 0.04		
VCB	MZ1:Brd2 ^{BD1}	24 \pm 8	-10.4 \pm 0.2	-7.3 \pm 0.2	-3.1 \pm 0.4	1.1 \pm 0.2	2.9	0.4 \pm 0.2
	MZ1:Brd2 ^{BD2}	28 \pm 3	-10.3 \pm 0.1	-10.5 \pm 0.1	0.2 \pm 0.2	1.07 \pm 0.02	2.3	0.36 \pm 0.06
	MZ1:Brd3 ^{BD1}	19 \pm 4	-10.6 \pm 0.1	-8.8 \pm 0.5	-1.8 \pm 0.7	1.01 \pm 0.01	3.5	0.5 \pm 0.1
	MZ1:Brd3 ^{BD2}	7 \pm 2	-11.2 \pm 0.2	-6.3 \pm 0.1	-4.9 \pm 0.3	0.99 \pm 0.04	10.7	1.0 \pm 0.2
	MZ1:Brd4 ^{BD1}	28 \pm 6	-10.3 \pm 0.1	-9.1 \pm 0.9	-1 \pm 1	0.97 \pm 0.06	2.3	0.4 \pm 0.1
	MZ1:Brd4 ^{BD2}	3.7 \pm 0.7	-11.5 \pm 0.1	-8.9 \pm 0.1	-2.6 \pm 0.2	1.02 \pm 0.02	17.6	1.24 \pm 0.09
	MZ1:Brd2 ^{BD1} KEA	12 \pm 7	-10.9 \pm 0.4	-5.7 \pm 0.2	-5.2 \pm 0.2	0.8 \pm 0.1	7.9	0.8 \pm 0.3
	MZ1:Brd4 ^{BD2} QVK	14.9 \pm 0.1	-10.68 \pm 0.03	-6.2 \pm 0.3	-4.5 \pm 0.3	0.9 \pm 0.1	4.2	0.62 \pm 0.04

508

509 All ITC titrations were performed at 25 °C. Values reported are the mean \pm S.E.M. from two independent measurements, except for
 510 VCB titration into MZ1 (line ^a) for which values reported are the mean \pm S.E.M. from eight independent measurements.

511

512 **Online Methods**

513

514 **Chemical synthesis:** Synthesis of compounds described in this paper and their intermediates
515 are described in the **Supplementary Note**.

516 **Constructs, protein expression and purification.** Wild-type and mutant versions of human
517 proteins VHL (UniProt accession number: P40337), ElonginC (Q15369), ElonginB
518 (Q15370), Brd2 (P25440), Brd3 (Q15059) and Brd4 (O60885) were used for all protein
519 expression. For expression of VCB, N-terminally His₆-tagged VHL (54–213), ElonginC (17–
520 112) and ElonginB (1–104) were co-expressed in *Escherichia coli* BL21(DE3) at 24 °C for
521 16 h using 3 mM isopropyl β-D-1-thiogalactopyranoside (IPTG). *E. coli* cells were lysed
522 using a pressure cell homogenizer (Stansted Fluid Power) and lysate clarified by
523 centrifugation. His₆-tagged VCB was purified on a HisTrapFF affinity column (GE
524 Healthcare) by elution with an imidazole gradient. The His₆ tag was removed using TEV
525 protease and the untagged complex dialysed into low concentration imidazole buffer. VCB
526 was then flowed through the HisTrapFF column a second time, allowing impurities to bind as
527 the complex eluted without binding. VCB was then additionally purified by anion exchange
528 and size-exclusion chromatography using MonoQ and Superdex-75 columns (GE
529 Healthcare), respectively. The final purified complex was stored in 20 mM Bis Tris, pH 7,
530 150 mM sodium chloride and 1 mM dithiothreitol (DTT). Brd2^{BD1} (71–194), Brd2^{BD2} (344–
531 455), Brd3^{BD1} (24–146), Brd3^{BD2} (306–416), Brd4^{BD1} (44–178) and Brd4^{BD2} (333–460) as
532 well as equivalent mutant constructs were expressed with an N-terminal His₆ tag in *E. coli*
533 BL21(DE3) at 18 °C for 20 h using 0.2 mM IPTG. His₆-tagged BDs were purified on nickel
534 Sepharose™ 6 fast flow beads (GE Healthcare) by elution with increasing concentrations of
535 imidazole. For crystallography the His₆-tagged BD was cleaved with TEV protease and
536 dialysed into low concentration imidazole buffer. The BD was then flowed over the nickel
537 beads a second time to remove impurities and protease. BDs were then additionally purified
538 by size-exclusion chromatography using a Superdex-75 column. For AlphaLISA, ITC and
539 ubiquitination reactions, following elution of His₆-tagged BDs from the nickel beads, the BDs
540 were purified by size-exclusion chromatography using a Superdex-75 column. The final
541 purified proteins were stored in 20 mM 4-(2-hydroxyethyl)-1-piperazineethanesulfonic acid
542 (HEPES), pH 7.5, 150 mM sodium chloride and 1 mM DTT. All chromatography
543 purification steps were performed using Äkta FPLC purification systems (GE Healthcare) or
544 glass econo-columns (Bio-Rad) at room temperature.

545 **Crystallography.** VCB, MZ1 and Brd4^{BD2} were mixed as a 1:1:1 stoichiometric ternary
546 complex with a final concentration of 10 mg/mL. Drops of the ternary complex were mixed
547 1:1 with 13% (w/v) PEG 8000 and 0.1 M sodium citrate (pH 6.3) in the hanging-drop vapour
548 diffusion format. Crystals appeared within minutes and were fully grown after one day. A
549 crystal was dehydrated in a solution containing 18% (w/v) PEG 8000 for a few minutes and
550 flash-cooled in liquid nitrogen using 20% 2-methyl-2,4-pentanediol in liquor solution as a
551 cryoprotectant. Diffraction data were collected at Diamond Light Source beamline I04-1
552 using a Pilatus 6M-F detector at a wavelength of 0.92819 Å. Indexing and integration of
553 reflections was performed using XDS with the XDSGUI interface⁴³, and scaling and merging
554 with AIMLESS⁴⁴ in CCP4i⁴⁵. The Wilson *B* factor was estimated at 47.2 Å². To solve the
555 phase problem the molecular replacement method was used with the program PHASER⁴⁶
556 using search models derived from the coordinates of VCB (PDB entry 1VCB²⁶) and Brd4^{BD2}
557 (PDB entry 2OUO²⁰). Two instances of the ternary complex were found in the asymmetric
558 unit, indicating a final solvent content of 68% as calculated from the Matthews coefficient.
559 The initial model was refined iteratively using REFMAC⁴⁷ and COOT⁴⁸. Ligand structures

560 and restraints were generated using the PRODRG server⁴⁹. The MOLPROBITY server⁵⁰ was
561 used to validate the geometry and steric clashes in the structures; the distribution of backbone
562 torsion angles in the Ramachandran plot are 98.3% in the favored region and 1.7% in the
563 allowed region. The structure has been deposited in the protein data bank (PDB) with
564 accession code 5T35 and data collection and refinement statistics are presented in
565 **Supplementary Table 1**. Interfaces and contacts observed in the crystal structure were
566 calculated with PISA⁵¹ and LIGPLOT⁵². All figures were generated using PyMOL.

567 **Molecular dynamics simulations.** MD simulations were carried out using the NAMD
568 program⁵³ and the CHARMM 36 force field⁵⁴. We attempted to derive *ab initio* topology and
569 parameter files for MZ1 using Jaguar v. 9.0 (Schrödinger Inc., LLC, New York, NY, US).
570 However, characterization of the minimized structure as a minimum by vibrational analysis
571 proved unsuccessful (number of imaginary frequencies > 0) using several approaches and
572 initial structures, probably due to the large number of atoms. Therefore topology and
573 parameter files were generated using the CGenFF server⁵⁵.

574 To simulate the Brd4^{BD2}:MZ1:VHL ternary complex in solution, the coordinates of the X-ray
575 crystal structure of the complex (chains A and D) were used as starting structure for
576 simulation. ElonginB and ElonginC, which are sufficiently far from the hydroxyproline
577 recognition site of VHL (> 20 Å), were excluded to increase computational efficiency
578 throughout the simulation. The model was solvated in a TIP3P water box with a padding of
579 12 Å from the edge of the box to any protein atom. The system charges were neutralized with
580 sodium or chloride ions as appropriate. The solvated system was minimized for 3,000 steps
581 with all protein and MZ1 atoms restrained to eliminate residual unfavorable interactions
582 between each other and the solvent, followed by another 5,000 steps with all atoms free to
583 move. Heating of the system from 0 to 300 K was achieved in 100 ps (time step of 1 fs), with
584 fixed protein backbone atoms to allow relaxation of the solvent. The system was
585 subsequently equilibrated for 600 ps (time step of 2 fs) with all atoms free to move. The NPT
586 ensemble was used during production simulation of 100 ns (time step of 2 fs). The
587 temperature was controlled with a Langevin thermostat at 300 K, and the pressure with a
588 Nose-Hoover Langevin piston barostat at 1 bar. A SHAKE constraint was applied to all
589 bonds containing hydrogen atoms. Short-range nonbonded interactions were switched at 10 Å
590 and cut off at 12 Å, and particle mesh Ewald summation was employed for long-range non-
591 bonded interactions.

592 The trajectory was analysed using VMD v. 1.9.2⁵⁶ and taking snapshots every 10 ps of
593 simulation, unless otherwise stated. To calculate *root-mean-square deviations (RMSD)*
594 throughout the simulation, ternary complexes were superposed to the crystallographic
595 complex using an in-house PyMOL script considering only Ca atoms of the VHL protein
596 within a shell of 10 Å from MZ1. This was implemented in order to diminish the effect of
597 structural rearrangements occurring far from the hydroxyproline recognition site of VHL
598 during the simulation arising from the absence of ElonginB and ElonginC. *Radius of gyration*
599 (R_g) of the ternary complex, *i.e.* the radius of a sphere with equivalent moment of inertia, was
600 computed using Carma⁵⁷ at each snapshot considering the protein backbone. *Buried surface*
601 *area (BSA)* upon complex formation, *i.e.* the difference in surface-accessible surface area
602 (SASA) between the formed complex and the unbound partners in the system, was computed
603 considering all protein atoms and a spherical probe of radius 1.4 Å. *Intermolecular contacts*,
604 *i.e.* pair-to-pair contacts between an amino acid in Brd4^{BD2} and VHL, were considered
605 formed if more than five atoms of the amino acid were at a distance closer than 4.0 Å from
606 the partner protein. Intermolecular contacts were computed using the Timeline plugin v. 2.3
607 as implemented in VMD. Per-residue and per-atom inter- and intramolecular interaction
608 energies ($E_{vdW + electrostatic}$) were computed using an in-house automated routine of the NAMD

609 Energy plugin v. 1.4 as implemented in VMD. Interaction energies were estimated by adding
 610 the pair-wise van der Waals and electrostatic contributions between individual amino acids or
 611 atoms and the corresponding partner. In the case of per-atom calculations, the interaction
 612 energies of hydrogen atoms were added to their corresponding heavy atom. For
 613 intramolecular interactions analysis, MZ1 was divided into three sections (JQ1, PEG linker,
 614 and VH032) and pair-wise energetic contributions from the atoms of each section to the rest
 615 of the molecule (excluding 1–4 bonded atoms) were calculated. In order to obtain comparable
 616 and interpretable results, the following scaling factor and cutoff value were applied to the
 617 electrostatic contribution:

$$\begin{cases} \text{if } |E_{vdW}| \geq 0.1: E_{\text{electrostatic}} = 0.07 * E_{\text{raw electrostatics}} \\ \text{if } |E_{vdW}| < 0.1: E_{\text{electrostatic}} = 0 \end{cases}$$

618 **Isothermal titration calorimetry (ITC)** Titrations were performed on an ITC200 micro-
 619 calorimeter (GE Healthcare). The titrations were all performed as reverse mode (protein in
 620 syringe, ligand in cell) and consisted of 19 injections of 2 μL protein solution (20 mM Bis-
 621 tris propane, 150 mM NaCl, 1 mM tris(2-carboxyethyl)phosphine (TCEP), 0.02 % DMSO,
 622 pH 7.4) at a rate of 2 sec/ μL at 120 s time intervals. An initial injection of protein (0.4 μL)
 623 was made and discarded during data analysis. All experiments were performed at 25 $^{\circ}\text{C}$,
 624 whilst stirring at 600 rpm. PROTACs (MZ1 or AT1) were diluted from a 10 mM DMSO
 625 stock solution to 20 μM in buffer containing 20 mM Bis-tris propane, 150 mM NaCl, 1 mM
 626 tris(2-carboxyethyl)phosphine (TCEP), pH 7.4. The final DMSO concentration was 0.01 or
 627 0.02 %. Bromodomain (100 or 200 μM , in the syringe) was titrated into the PROTAC (10 or
 628 20 μM , in the cell). At the end of the titration, the excess of solution was removed from the
 629 cell, the syringe was washed and dried, VCB complex (84 or 168 μM , in the same buffer)
 630 was loaded in the syringe and titrated into the complex PROTAC:bromodomain. The
 631 concentration of the complex in the cell (C) after the first titration (8.4 or 16.8 μM), was
 632 calculated as follow:

$$C = \frac{C_0 \cdot V_{\text{cell}}}{V_{\text{cell}} + V_{\text{inj}}}$$

633 where: C_0 is the initial concentration of the PROTAC in the cell (20 μM), V_{cell} is the volume
 634 of the sample cell (200.12 μL) and V_{inj} is the volume of titrant injected during the first
 635 titration (38.4 μL). Titrations for the binary complex PROTAC:VCB were performed as
 636 follow: to the solution of PROTAC (10 or 20 μM , in the cell), buffer (38.4 μL) was added by
 637 means of a single ITC injection. The excess of solution was removed from the cell, the
 638 syringe was washed and dried, VCB complex (84 or 168 μM , in the same buffer) was loaded
 639 in the syringe and titrated into the diluted PROTAC solution. The data were fitted to a single
 640 binding site model to obtain the stoichiometry n , the dissociation constant K_d and the
 641 enthalpy of binding ΔH using the Microcal LLC ITC200 Origin software provided by the
 642 manufacturer. The reported values are the mean \pm s.e.m. from independent measurements
 643 (eight for VCB into MZ1; seven for VCB into AT1; two for each BD into VCB:PROTAC).

644 **Simulations of ternary complex fractions.** Fractions of ternary complexes were calculated
 645 by applying the ternary equilibria model in the excel spreadsheet provided in ref. ²³. Input
 646 parameters were $[\text{VHL}]_t = [\text{BD}]_t = 40 \text{ nM}$; $K_d(\text{VHL}) = 66 \text{ nM}$; K_d and α (BD) were as
 647 measured by ITC (**Table 1**).

648 **Biotinylation of VCB.** To biotinylate VCB the complex was mixed in a 1:1 stoichiometry
649 with EZ-Link NHS-PEG₄-Biotin (Thermo Scientific) and incubated at room temperature for
650 1 h. To remove any unreacted NHS-biotin the sample was run over a PD-10 desalting column
651 (GE Healthcare) into 20 mM HEPES, pH 7.5, 150 mM sodium chloride and 1 mM DTT.

652 **AlphaLISA assays.** All assays were performed at room temperature and plates sealed with
653 transparent film between addition of reagents. All reagents were diluted in 50 mM HEPES,
654 pH 7.5, 100 mM NaCl, 0.1% (w/v) bovine serum albumin and 0.02% (w/v) 3-[(3-
655 cholamidopropyl)dimethylammonio]-1-propanesulfonate (CHAPS) and each solution was
656 prepared as a 5× stock and mixed into a final volume of 25 μL per well. Each protein sample
657 (biotinylated VCB and His₆-BD) and PROTAC were mixed and incubated for 1 h. Ni-coated
658 acceptor beads were added and plates incubated another 1 h. Streptavidin-coated donor beads
659 were added and plates incubated for a final 1 h. Plates were read on a PHERAstar FS (BMG
660 Labtech) using an optic module with an excitation wavelength of 680 nm and emission
661 wavelength of 615 nm. Within each read there was a settling time of 0.1 s, an excitation time
662 of 0.3 s and an integration time of 0.6 s. For BET-BD titration experiments, VCB and
663 PROTACs or Biotin-JQ1 alone were kept constant at a final concentration of 20 nM and
664 His₆-BD was serially diluted three-in-five from 200 nM. For VCB/Biotin-JQ1 titration
665 experiments, His₆-BDs and PROTACs were kept constant at a final concentration of 40 nM
666 and VCB or Biotin-JQ1 was serially diluted one-in-two from 200 nM. The intensity values
667 were plotted with concentration values on a log₁₀ scale.

668 **Tissue culture.** Human HeLa cell lines were obtained from ATCC and were kept in DMEM
669 medium (Gibco) supplemented with 10% FBS (Gibco), L-glutamate (Gibco), penicillin and
670 streptomycin. Cells were kept in incubator at 37 °C, 5% CO₂. All cell lines were tested for
671 mycoplasma contamination every month using MycoAlert™ Mycoplasma detection kit
672 (Lonza).

673 **Cell treatment and lysis.** HeLa cells were seeded at 2.5×10⁵ per well on a standard six-well
674 plate. After a day, cells were treated with test compounds for the desired period of time. Cells
675 were washed with PBS twice before lysis. Lysis was achieved by applying RIPA buffer
676 (Sigma), supplemented with 1× protease inhibitor cocktail (Roche), Benzamide (Merck) and
677 0.5 mM MgCl₂ to the cells on ice. Lysate was briefly sonicated and then centrifuged at
678 20,000 × g for 10 min at 4 °C. Supernatant was collected as cell extract and protein
679 concentration was measured by BCA assay. The extract was snap frozen in liquid nitrogen
680 for storage before being used for Western blot analysis. Cycloheximide (C7698, Sigma
681 Aldrich) was used at 100 μg/mL for the indicated times.

682 **Western blot.** Blots were probed with antibodies for Brd4 (AbCam ab128874, 1:1,000
683 dilution), Brd3 (AbCam ab50818, 1:500 dilution), Brd2 (AbCam ab139690, 1:2,000
684 dilution), β-actin (AbCam ab8227, 1:2,000 dilution) and cMyc (AbCam ab32072, 1:1,000
685 dilution) antibodies. Blots were developed with anti-Mouse or anti-Rabbit IRDye® 800CW
686 secondary antibody from Licor (1:10,000 dilution) and bands visualized using Licor Odyssey
687 Sa imaging system. Image processing and band intensity quantification were done using
688 Licor Image Studio software Version 5.2.5. Ubiquitination blots were probed with anti-6×His
689 antibody (AbCam ab18184, 1:2,000 dilution) and then with Anti-mouse IgG, HRP-linked
690 Antibody (Cell Signaling technology #7076, 1:2,000 dilution). Probed blots were visualised
691 with ECL Western Blotting Substrate (Pierce #32106) on film.

692 **Sample preparation for MS proteomics.** HeLa cells were seeded at 2×10^6 on a 100mm
693 plate 24 h before treatment. To treat the cells, culture medium was replaced with 12 mL of
694 medium containing the test compound. After 24 h, medium was removed and cells were
695 washed with 12 mL of cold PBS twice. Samples were kept on ice from this point onwards.
696 Cells were lysed in 0.5 mL of 100 mM Tris pH 8.0, 4% (w/v) SDS supplemented with
697 protease inhibitor cocktail (Roche). The lysate was pulse sonicated briefly and then
698 centrifuged at $17,000 \times g$ for 15 min at 4 °C. The supernatant fraction of cell extract was
699 snap-frozen in liquid nitrogen and stored in -80 °C freezer before further processing.

700 **Sample preparation for MS proteomics.** Samples were quantified using a micro BCA
701 protein assay kit (Thermo Fisher Scientific) and 200µg of each sample was processed and
702 digested using the Filter Aided Sample Preparation (FASP) method⁵⁸. The samples were then
703 desalted using a 7 mm, 3 ml C18 SPE cartridge column (EmporeTM, 3M) and labelled with
704 TMT⁵⁹ 10plexTM Isobaric Label Reagent Set (Thermo Fisher Scientific) as per manufacturers
705 instructions. After labelling, the peptides from the 10 samples were pooled together in equal
706 proportion. The pooled sample was fractionated into 20 discrete fractions using high pH
707 reverse phase chromatography⁶⁰ on a XBridge peptide BEH column (130 Å, 3.5 µm 2.1 X
708 150 mm, Waters) using an Ultimate 3000 HPLC system (Thermo Scientific/Dionex). Column
709 temperature was set to 20 °C. The peptides were separated using a mix of buffers A (10 mM
710 ammonium formate in water, pH 10) and B (10 mM ammonium formate in 90% CH₃CN, pH
711 10). The peptides were eluted from the column using a flow rate of 200 µl/min and a linear
712 gradient from 5% to 60% buffer B over 60 min. The peptides eluted from the column were
713 separated into 40 fractions prior to concatenation into 20 fractions based on the UV signal of
714 each fraction. All the fractions were dried in a speedvac concentrator and resuspended in 10
715 µl 5% formic acid, then diluted to 1% prior to MS analysis.

716 **nLC-MS/MS analysis.** The fractions were analysed sequentially on a Q ExactiveTM HF
717 Hybrid Quadrupole-OrbitrapTM Mass Spectrometer (Thermo Scientific) coupled to an
718 Ultimate 3000 RSLC nano UHPLC system (Thermo Scientific) and Easyspray column (75
719 µm × 50 cm, PepMap RSLC C18 column, 2 µm, 100 Å, Thermo Scientific). The peptides
720 from each fraction were separated using a mix of buffer A (0.1% formic acid in MS grade
721 water) and B (0.08% formic acid in 80% MS grade CH₃CN). The peptides from each fraction
722 were eluted from the column using a flow rate of 300 nl/min and a linear gradient from 5% to
723 40% buffer B over 122 min. The column temperature was set at 50 °C. The Q ExactiveTM HF
724 Hybrid Quadrupole-OrbitrapTM Mass Spectrometer was operated in data dependent mode
725 with a single MS survey scan followed by 10 sequential m/z dependant MS2 scans. The 10
726 most intense precursor ions were sequentially fragmented by Higher energy Collision
727 Dissociation (HCD). The MS1 isolation window was set to 0.4 Da and the resolution set
728 120,000. MS2 resolution was set as 60,000. The maximum ion injection time for MS1 and
729 MS2 were set at 50 msec and 200 msec, respectively.

730 **Peptide and protein identification.** The raw ms data files for all 20 fractions were merged
731 and searched against the Sprot database with taxonomy set to *Homo sapiens* by Proteome
732 Discoverer Version 1.4 (Thermo Scientific) using the Mascot v.2.4.1 (Matrix Science) search
733 engine for protein identification and TMT reporter ion quantitation. The identification was
734 based on the following database search criteria: enzyme used Trypsin/P; maximum number of
735 missed cleavages equal to 2; precursor mass tolerance equal to 10 ppm; fragment mass
736 tolerance equal to 0.06 Da; dynamic modifications: Oxidation (M), Dioxidation (M), Acetyl
737 (N-term), Gln->pyro-Glu (N-term Q), Pro->Hyp (P), Deamidation(N,Q); static modifications:

738 Carbamidomethyl (C), TMT10plex (K), TMT10plex (N-term). For protein identification the
739 mascot ion score threshold was set at 30 and a minimum of 2 peptides was required.

740 **Peptide and protein quantitation.** The ratios of TMT reporter ion abundances in MS/MS
741 spectra generated by HCD from raw data sets were used for TMT quantification. Isotopic
742 correction factors were applied for the batch of TMT reagents used in this experiment as per
743 manufacturers recommendation. A minimum of two unique peptides was used for
744 quantitation and the resultant ratios were normalized based on protein median. Quantified
745 proteins were filtered if the absolute fold change difference between the two DMSO
746 replicates was ≥ 1.3 .

747 **Model construction of the multisubunit CRL2^{VHL}-MZ1-Brd4 complex.** A structural
748 model of the CRL2^{VHL} (VHL-EloC-EloB-Cul2-Rbx1) with bound MZ1-Brd4^{BD2} at one end
749 and E2-Ubiquitin at the other end was constructed in PyMOL by aligning our Brd4^{BD2}-
750 MZ1-VHL-EloC-EloB on to the quaternary structure VHL-EloC-EloB-Cul2^{NTD} (PDB
751 entry 4WQO). Cul2^{NTD} and Cul2^{CTD} were modelled based on the structures of Cul5^{NTD} (PDB
752 entry 2WZK) and Cul1^{CTD}-Rbx1 (PDB entry 3RTR) and superposed onto full-length Cul1
753 from PDB entry 1LDK. Finally, the Rbx1-E2-Ub arm was modelled based on the crystal
754 structure of Rbx1-Ubc12~NEDD8-Cul1-Dcn1 (PDB entry 4P5O) superposed via the cullin
755 subunit.

756 **Recombinant ubiquitination experiments and ubiquitination site identification.** His₆-
757 tagged BET-BDs (2 μ M) were ubiquitinated in the presence of E1 Ube1 (19 nM), E2 Ube2d1
758 (145 nM), ubiquitin (Ubiquigent, 1 mg/mL), recombinant VHL-ElonginC-ElonginB-Cullin2-
759 Rbx1 complex (330 nM) and MZ1 (2 μ M) standing for 24 h at room temperature in a buffer
760 of 25 mM HEPES, pH 7.5, 5 mM MgCl₂, 100 mM NaCl, 2 mM ATP, 0.1 mg/mL BSA and 1
761 mM TCEP. Reactions were terminated by the addition of 1 \times NuPAGE LDS sample buffer
762 (Invitrogen).

763 **Sample preparation for MS.** Samples were run 1–2 cm into a pre-cast 4–12% Bis-Tris
764 NuPAGE gel and the entire protein content of each lane excised, washed and dried. Proteins
765 were reduced with 10 mM DTT and 20 mM ammonium carbonate at 56 °C for 60 min and
766 then alkylated with 50 mM N-ethylmaleimide and 20 mM ammonium carbonate at room
767 temperature for 30 min. Proteins were trypsinized overnight at 30 °C and the resulting
768 peptides extracted and dried down.

769 **nLC-MS/MS analysis.** Each peptide sample was reconstituted in 10 μ l 5% formic acid then
770 diluted to 1% prior to MS analysis. Peptide samples were injected onto a C18 PepMap 100
771 (300 μ m x 5 mm, Thermo Scientific) trap column with buffer A (0.1% formic acid in MS
772 grade water) using an Ultimate 3000 RSLC nano UHPLC system. After a 5 min wash at 5
773 μ l/min the sample was then eluted onto an EasySpray PepMap RSLC C18 column (75 μ m x
774 50 cm, Thermo Scientific) into a LTQ Orbitrap Velos Pro via an EasySpray ion source. The
775 peptides were eluted from the column using a flow rate of 300 nl/min and a linear gradient
776 from 2% to 40% buffer B (0.08% formic acid in 80% MS grade CH₃CN) over 124 min. The
777 column temperature was set at 50 °C. The Orbitrap Velos Pro ms system was operated in
778 data dependant acquisition mode using a Top 15 method with Lockmass = 445.120024. A
779 MS1 survey scan with a range of 335–1800 m/z and a resolution of 60,000 was followed by
780 15 sequential MS2 scans at the normal scan rate using the LTQ Velos ion trap. The FTMS
781 and ITMS AGC targets were set to 1e⁶ ions and 5e³ ions respectively. The FTMS and ITMS
782 maximum fill times were set to 500 msec and 100 msec respectively. ITMS isolation width

783 was set at 2 Da with a normalised collision energy of 35, a default charge state of 2, an
784 Activation Q of 0.250 and Activation Time of 10 msec.

785 **Peptide and protein identification.** The resultant raw data was searched against the Sprot
786 database with a taxonomy filter set to *H. sapiens* using the Mascot v. 2.4.1 (Matrix Science)
787 search engine to identify peptides containing Lysines with εN-linked di-glycine
788 modifications. Peptide mass tolerance was set to 10 ppm and the fragment mass tolerance set
789 to 0.6 Da. The number of maximum miss-cleavages was set to 2. The enzyme was set to
790 Trypsin/P and the following variable modifications were considered: Acetyl (N-term),
791 Deamidated (NQ), Dioxidation (M), Gln->pyro-Glu (N-term Q), GlyGly (K), Oxidation (M).
792 A fixed modification for Cysteine was set to N-ethylmaleimide. A mascot ion score threshold
793 was set at 37 to filter non-significant peptide identifications.

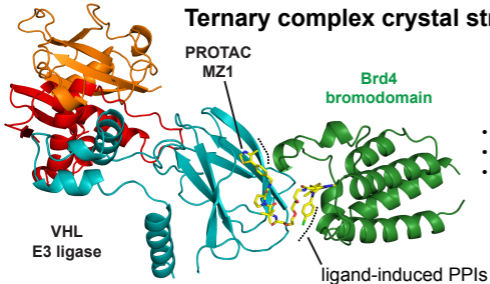
794 **Statistical methods.** No statistical methods were used to predetermine sample size. The
795 experiments were not randomized, and the investigators were not blinded to allocation during
796 experiments and outcome assessment. For all experiments, number of replicates (*n*), mean
797 value, error value and P value cutoffs are described in the respective figure legends. Error
798 bars are shown for all data points with replicates as a measure of variation with the group. All
799 *t*-tests performed were two-tailed *t*-tests assuming equal variances.

800

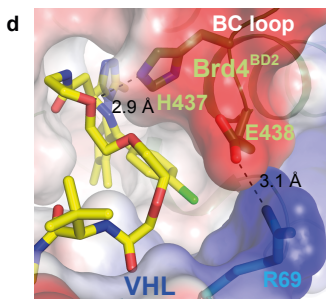
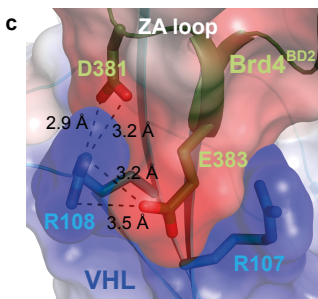
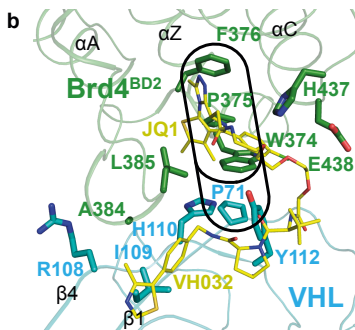
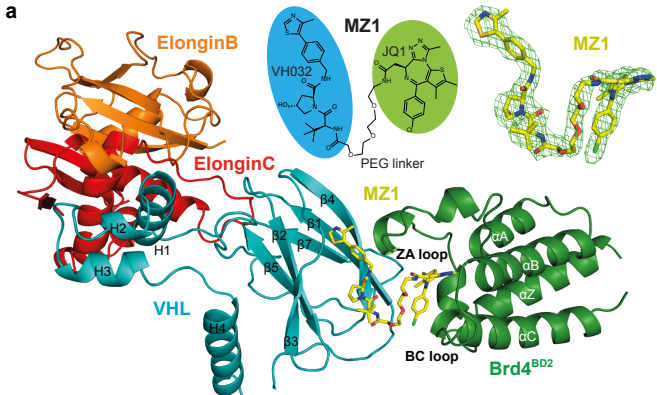
- 801 43. Kabsch, W. XDS. *Acta Crystallogr D Biol Crystallogr* **66**, 125–132 (2010).
802 44. Evans, P. R. & Murshudov, G. N. How good are my data and what is the resolution?
803 *Acta Crystallogr D Biol Crystallogr* **69**, 1204–1214 (2013).
804 45. Winn, M. D. *et al.* Overview of the CCP4 suite and current developments. *Acta*
805 *Crystallogr D Biol Crystallogr* **67**, 235–242 (2011).
806 46. McCoy, A. J. *et al.* Phaser crystallographic software. *J Appl Crystallogr* **40**, 658–674
807 (2007).
808 47. Murshudov, G. N. *et al.* REFMAC5 for the refinement of macromolecular crystal
809 structures. *Acta Crystallogr D Biol Crystallogr* **67**, 355–367 (2011).
810 48. Emsley, P., Lohkamp, B., Scott, W. G. & Cowtan, K. Features and development of
811 Coot. *Acta Crystallogr D Biol Crystallogr* **66**, 486–501 (2010).
812 49. Schüttelkopf, A. W. & van Aalten, D. M. F. PRODRG: a tool for high-throughput
813 crystallography of protein-ligand complexes. *Acta Crystallogr D Biol Crystallogr* **60**,
814 1355–1363 (2004).
815 50. Chen, V. B. *et al.* MolProbity: all-atom structure validation for macromolecular
816 crystallography. *Acta Crystallogr D Biol Crystallogr* **66**, 12–21 (2010).
817 51. Krissinel, E. & Henrick, K. Inference of macromolecular assemblies from crystalline
818 state. *J Mol Biol* **372**, 774–797 (2007).
819 52. Laskowski, R. A. & Swindells, M. B. LigPlot+: multiple ligand-protein interaction
820 diagrams for drug discovery. *J Chem Inf Model* **51**, 2778–2786 (2011).
821 53. Phillips, J. C. *et al.* Scalable molecular dynamics with NAMD. *J.Comput.Chem.* **26**,
822 1781–1802 (2005).
823 54. Brooks, B. R. *et al.* CHARMM: the biomolecular simulation program.
824 *J.Comput.Chem.* **30**, 1545–1614 (2009).
825 55. Vanommeslaeghe, K. & Mackerell, A. D. Automation of the CHARMM General
826 Force Field (CGenFF) I: bond perception and atom typing. *J Chem Inf Model* **52**,
827 3144–3154 (2012).
828 56. Humphrey, W., Dalke, A. & Schulten, K. VMD: visual molecular dynamics.

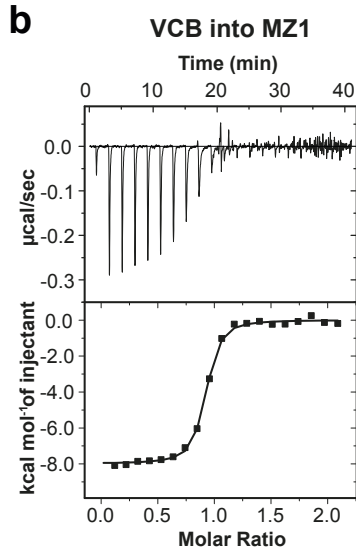
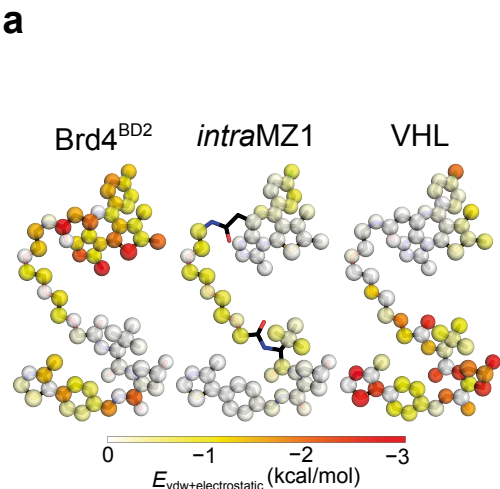
- 829 *J.Mol.Graphics* **14**, 33–8–27–8 (1996).
- 830 57. Glykos, N. M. Software news and updates. Carma: a molecular dynamics analysis
831 program. *J.Comput.Chem.* **27**, 1765–1768 (2006).
- 832 58. Manza, L. L., Stamer, S. L., Ham, A.-J. L., Codreanu, S. G. & Liebler, D. C. Sample
833 preparation and digestion for proteomic analyses using spin filters. *Proteomics* **5**,
834 1742–1745 (2005).
- 835 59. Thompson, A. *et al.* Tandem mass tags: a novel quantification strategy for comparative
836 analysis of complex protein mixtures by MS/MS. *Anal.Chem.* **75**, 1895–1904 (2003).
- 837 60. Gilar, M., Olivova, P., Daly, A. E. & Gebler, J. C. Orthogonality of separation in two-
838 dimensional liquid chromatography. *Anal.Chem.* **77**, 6426–6434 (2005).

Ternary complex crystal structure

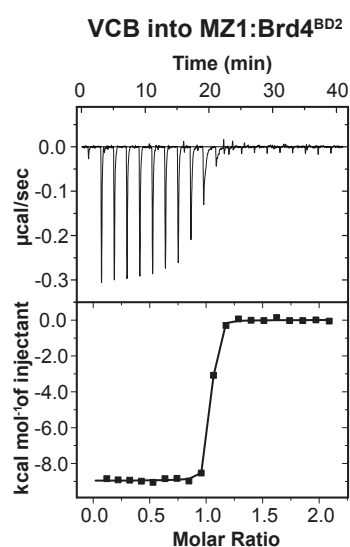


- Cooperative and stable
- Highly populated
- **Selective degradation**

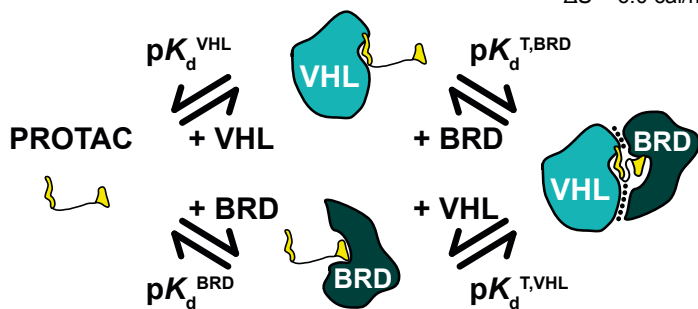




$N = 0.880 \pm 0.004$ sites
 $K_d = 67 \pm 8$ nM
 $\Delta H = -7,980 \pm 60$ cal/mol
 $\Delta S = 6.0$ cal/mol/deg



$N = 0.991 \pm 0.001$ sites
 $K_d = 4.4 \pm 1.0$ nM
 $\Delta H = -8,960 \pm 30$ cal/mol
 $\Delta S = 8.2$ cal/mol/deg



$$\alpha = \frac{K_d^A}{K_d^{T,A}}; \Delta pK_d = pK_d^{T,A} - pK_d^A, \text{ cooperativity}$$

$\alpha < 1; \Delta pK_d < 0$, negative cooperativity

$\alpha = 1; \Delta pK_d = 0$, no cooperativity

$\alpha > 1; \Delta pK_d > 0$, positive cooperativity

